

The Opacity of Spiral Galaxy Disks VIII: Structure of the Cold ISM

B. W. Holwerda¹, B. Draine², K.D. Gordon³, R. A. González⁴, D. Calzetti⁵, M. Thornley⁶, B. Buckalew⁷, Ronald J. Allen¹ and P. C. van der Kruit⁸

holwerda@stsci.edu

ABSTRACT

The quantity of dust in a spiral disk can be estimated using the dust's typical emission or the extinction of a known source. In this paper, we compare two techniques, one based on emission and one on absorption, applied on sections of fourteen disk galaxies. The two measurements reflect, respectively the average and apparent optical depth of a disk section. Hence, they depend differently on the average number and optical depth of ISM structures in the disk.

The small scale geometry of the cold ISM is critical for accurate models of the overall energy budget of spiral disks. ISM geometry, relative contributions of different stellar populations and dust emissivity are all free parameters in galaxy Spectral Energy Distribution (SED) models; they are also sometimes degenerate, depending on wavelength coverage. Our aim is to constrain typical ISM geometry.

The apparent optical depth measurement comes from the number of distant galaxies seen in HST images through the foreground disk, calibrated with the

¹Space Telescope Science Institute, Baltimore, MD 21218, USA

²Dept. of Astrophysical Sciences, Princeton University, Princeton, NJ 08544-1001, USA

³Steward Observatory/Department of Astronomy, University of Arizona, Tucson, AZ 85721 USA

⁴Centro de Radioastronomía y Astrofísica, Universidad Nacional Autónoma de México, 58190 Morelia, Michoacán, Mexico

⁵University of Massachusetts, Department of Astronomy, 710 North Pleasant Street, Amherst, MA 01003

⁶Department of Physics & Astronomy, Bucknell University, Lewisburg, PA 17837

⁷Dept. of Physics, Embry-Riddle University, 3700 Willow Creek Rd, Prescott, AZ 86301, USA

⁸Kapteyn Astronomical Institute, P.O. Box 800, Groningen, the Netherlands

“Synthetic Field Method” (SFM). We discuss what can be learned from the SFM measurement alone regarding ISM geometry.

We measure the IR flux in images from the *Spitzer* Infrared Nearby Galaxy Survey in the same section of the disk that was covered by HST. A physical model of the dust is fit to the SED to estimate the dust surface density, mean temperature, and brightness in these disk sections. The surface density is subsequently converted into the average optical depth estimate.

The two measurements generally agree and the SED in order model finds a mostly cold dust ($T < 25$ K.). The ratios between the measured average and apparent optical depths of the disk sections imply optically thin ($\tau_c = 0.4$) clouds in these disks. Optically thick disks, are likely to have more than a single cloud along the line-of-sight.

Subject headings: (ISM:) dust, extinction, ISM: structure, galaxies: ISM, galaxies: spiral, infrared: galaxies, infrared: ISM

1. Introduction

The dust content of a spiral galaxy disk can be mapped either by the characteristic dust emission in the far-infrared (FIR) and sub-mm regimes, or by using the attenuation of known background sources. Both techniques have seen recent significant improvements in accuracy and sensitivity, with complementary results shedding light on the dusty interstellar medium in spiral disks.

The emission from the interstellar dust in the disks of spiral galaxies has been characterized with increasing accuracy by several infrared space missions (IRAS, ISO and, recently, *Spitzer*), as well as the sub-mm observations of SCUBA on the JCMT. The improvements in spatial resolution and wavelength coverage have led to significant insight into the temperature components of the dust in spiral disks, and into the relation between dusty clouds and star-formation. The FIR emission from spiral galaxies has revealed that the dust can be described by two dominant thermal components: warm ($25 \text{ K} < T < 100 \text{ K}$) and cold ($T < 25 \text{ K}$). Both the warm and cold components can be found in spiral arms, and there is a smooth disk of cold dust between these arms. Most of the dust mass in the spiral disk is cold (see the review articles by Genzel & Cesarsky 2000; Tuffs & Popescu 2005; Popescu & Tuffs 2005).

FIR and sub-mm observations of galaxies find indications (e.g., Trewhella et al. 2000; Alton et al. 1998) or direct evidence of cold dust disks extending beyond the stellar disk

(Nelson et al. 1998; Davies et al. 1999; Popescu & Tuffs 2003). The studies of edge-on spirals by Radovich et al. (2001) and Xilouris et al. (1999) quantified the radial profile as a scalelength of the dust that is 40% larger than that of the starlight. The contribution of the cold ISM ($T < 25$ K) to the overall emission of spiral disks has been difficult to constrain because of the degeneracy between dust temperature and mass. Hence, the cold ISM’s relation with HI and their relative distribution remain unknown.

Spitzer observations, mostly from the Spitzer Infrared Nearby Galaxy Survey (SINGS, Kennicutt et al. 2003), have already contributed greatly to the understanding of spiral disks. The relations between the tracers of cold dust (70 and 160 micron emission) and star-formation, both obscured (24 micron) and unobscured (UV and H α emission) have already been studied with this multi-wavelength survey in several canonical galaxies and their substructure: the starburst M51 (Calzetti et al. 2005; Thornley et al. 2006), the grand design spiral M81 (Gordon et al. 2004; Pérez-González et al. 2006), the rings of NGC 7331 (Regan et al. 2004) and M31 (Gordon et al. 2006), the superwind in M82 (Engelbracht et al. 2006), and the dwarf NGC 55 (Engelbracht et al. 2004). Dale et al. (2005, 2007) discuss the SED of all SINGS galaxies over all available wavelengths. Draine et al. (2007) find ample evidence for dust in all the SINGS galaxies, with the gas-to-dust ratio related to the metallicity. They find no evidence for very cold ($T < 10$ K) dust, however.

These studies find ample evidence of cold dust throughout the optical disks of spirals but, interestingly, also outside them in various places: on the edge of the optical disk (Thornley et al. 2006; Gordon et al. 2006), outside M82’s superwind (Engelbracht et al. 2006) and extending beyond the stellar disk (Hinz et al. 2006).

Parallel to these investigations of dust emission has gone an observational effort to quantify the absorption by dust in spiral disks using known background sources. White & Keel (1992) proposed using occulting galaxy pairs for this purpose. Nearby occulting galaxy pairs were initially investigated with ground-based data, both images (Andredakis & van der Kruit 1992; Berlind et al. 1997; Domingue et al. 1999; White et al. 2000) and spectra (Domingue et al. 2000). Subsequently, with the Hubble Space Telescope (HST), a more detailed picture of dust in these nearby disks emerged (Keel & White 2001a,b; Elmegreen et al. 2001). The results of these studies are that extinction is gray¹ when measured over disk sections greater than 100 pc, but resembles the Galactic extinction law at smaller scales – those that can only be resolved with HST. Arms are found to be more opaque than the general disk, and

¹Gray extinction is equal attenuation at all wavelengths: there is no relation between color and measured optical depth. A color measurement is dominated by the lines-of-sight with the *least* extinction, while the independent extinction measure is dominated by those with the *most* extinction. In cases where many lines-of-sight are mixed, gray extinction is mimicked.

some evidence suggests that the dust disk is a fractal, similar to the HI disk.

González et al. (1998) investigated the use of the calibrated number of distant galaxies seen through the foreground disk in HST images. The calibrated counts of distant galaxies have been explored further in the previous papers in this series (González et al. 1998, 2003; Holwerda et al. 2005a,b,c,d,e, 2006). Both the occulting galaxy technique and counts of distant objects yield very similar opacities for disks and spiral arms (Holwerda et al. 2005b).

In recent years, models have been developed to explain the Spectral Energy Distribution (SED) of edge-on spirals spanning wavelengths ranging from the UV to the FIR. (e.g., Popescu et al. 2000; Misiriotis et al. 2001; Popescu et al. 2000; Misiriotis et al. 2001; Tuffs et al. 2004; Boissier et al. 2004; Dasyra et al. 2005; Tuffs et al. 2004; Dasyra et al. 2005; Calzetti et al. 2005; Dopita et al. 2006b,a; Draine & Li 2007; Draine et al. 2007). Three scenarios have been proposed to explain the discrepancy between the apparent absorption in UV and optical wavelengths and the emission of dust in the FIR and sub-mm regimes:

1. A young stellar population is embedded in the dense plane of the disk. This is proposed by Popescu et al. (2000) and corroborated by Driver et al. (2007). The embedded young stars pump the FIR emission radiated by the dust plane.
2. A strongly clumped dusty medium. The clumping would lead to underestimate the dust mass from optical extinction in edge-on systems (Bianchi et al. 2000b; Witt & Gordon 2000; Misiriotis & Bianchi 2002); the dust mass would also be underestimated by a UV to FIR SED (Bianchi et al. 2000a).
3. A different emissivity of the cold dust grains –higher than canonical– in the FIR and sub-mm. A change of emissivity has been proposed for denser ISM regions (Alton et al. 2004; Dasyra et al. 2005) or, alternatively, for the lower density regions of the disk (Bendo et al. 2006).

In all three of these scenarios, the clumpiness of the dusty ISM is an important factor.

While in some models the large scale structure of the dusty ISM has been somewhat constrained (e.g., Xilouris et al. 1999; Seth et al. 2005; Bianchi 2007; Kamphuis et al. 2007), the small-scale geometry (“clumpiness”) of the cold ISM remains unknown. Therefore, an estimate of the prevalent dusty cloud size for spiral disks would provide a constraint for the SED models of spiral disks.

Given that SED and extinction techniques are sensitive to different characteristics of the dusty clouds in the spiral disk, a comparison between the optical depth derived from

these two methods has the potential to figure out the structure of the dusty ISM. Here, we compare the *I*-band optical depths for a section of the spiral disk, one derived from a SED model of the *Spitzer* fluxes (“average”), and one determined from the number of distant galaxies found in an HST image (“apparent”). The term “average” refers to what the optical depth proportional to the dust mass, uniformly distributed over the disk section. The term “apparent” means the effective optical depth of the disk section for a background uniform light source (original definitions from Natta & Panagia 1984). The term “opacity” is used throughout our previous papers for the apparent optical depth measured over a section of the disk for its whole height.

This paper is structured as follows: §2 discusses the *Spitzer* and HST data used. In §3, the two different methods to derive optical depths are presented. We discuss the relation between dust geometry and galaxy counts in §4. In §5, we present the derived optical depths; §6 presents a simple geometric model to interpret the results, and §7 lists our conclusions and future work.

2. Data

The data for this paper come from two archives, the HST archive and the fourth data release (SINGS team 2006) of the *Spitzer Infrared Nearby Galaxy Survey* (SINGS, Kennicutt et al. 2003)². There is an overlap of fourteen galaxies between the SINGS sample and that of Holwerda et al. (2005b). Two of these, NGC 3621 and NGC 5194, have two WFPC2 exposures analyzed in Holwerda et al. (2005b). The HST/WFPC2 data reduction is described in Holwerda et al. (2005a). The reasoning behind the HST sample selection from the archive is explained in §3.1.

The overlap between HST and *Spitzer* data is illustrated in Figure 1, with the WFPC2 footprint projected on the 24 micron *Spitzer* images. Only the solid angle covered by the WF chips is used for further analysis (the PC chip is excluded).

The Infrared Array Camera (IRAC) mosaic is made with the custom *SINGSdither* script, by M. Regan, that combines the scan images into a single mosaic using the “drizzle” algorithm (Fourth Data Release Notes, SINGS team 2006). The Multiband Imaging Photometer for *Spitzer* (MIPS) data products are calibrated, sky-subtracted mosaics in all three bands, reduced as described in Gordon et al. (2005); Bendo et al. (2006); SINGS team (2006). The basic instrument parameters, pixel scale, and adopted PSF FWHM for the seven main *Spitzer*

²<http://sings.stsci.edu>

imaging modes are summarized in Table 1.

3. Analysis

Two parallel estimates of the optical depth of disks are used in this paper: first, the apparent optical depth of the spiral disks is determined from the number of distant galaxies identified in the HST/WFPC2 images, calibrated with the “Synthetic Field Method” (SFM). Secondly, the optical depth of the same section of the spiral disks is derived from the dust surface density, which is a result of the SED model fit to the *Spitzer* fluxes using the model from Draine & Li (2007).

3.1. Galaxy counts: “Synthetic Field Method”

In principle, the number of distant galaxies seen through a spiral disk is a function of the dust extinction, as well as the crowding and confusion by the foreground disk. Initial applications of the number of distant galaxies as an extinction tracer were on the Magellanic Clouds (Shapley 1951; Wesselink 1961; Hodge 1974; MacGillivray 1975), but they lacked accuracy. The “Synthetic Field Method” (SFM) was developed by González et al. (1998) to correct an extinction measurement based on the number of distant galaxies in an HST image, for the effects of crowding and confusion by the foreground spiral disk.

The “Synthetic Field Method” follows a series of steps. First, the number of distant galaxies in an HST science field is determined. Second, a series of simulated (“synthetic”) fields are made. In each of these fields, a typical background (e.g., the Hubble Deep Field) is first dimmed by a gray screen and added to the science field. Third, the added distant objects are identified in these synthetic fields. The fourth step is to measure the relationship between the number of these identified synthetic distant galaxies and background dimming. From this relation and the original number of actual distant galaxies found in the science field, an average opacity can be found. It is important to remake the synthetic fields for each science field because the crowding and confusion issues are unique in each case.

An additional uncertainty in the resulting average extinction measurement is the cosmic variance in the intrinsic number of distant galaxies behind the foreground disk. The uncertainty due to cosmic variance can be estimated from the two-point correlation function of distant galaxies and folded into the Poissonian error. The cosmic variance uncertainty is of the same order as the Poisson statistical error for small numbers (For a complete discussion on the uncertainties of the SFM, see Holwerda et al. 2005a). Therefore, single-field

SFM measurements remain uncertain, but a meaningful conclusion can be drawn from a combined set of science fields.

We have applied this method successfully on archival WFPC2 data. Holwerda et al. (2005b) present the average radial opacity profile of spiral disks and the effect of spiral arms. The spiral arms are more opaque and show a strong radial dependence, while the more transparent disk shows a flat profile. Holwerda et al. (2005c) compare HI radial profiles to the opacity ones, and conclude that no good relation between disk opacity and HI surface density radial profiles can be found. However, Holwerda et al. (2005c) find that the sub-mm profile from Meijerink et al. (2005) generally agrees with their opacity measurements of M51. Holwerda et al. (2005e) compare the relation between surface brightness and disk opacity; this relation is strong in the spiral arms, but weak in the rest of the disk.

González et al. (2003) predicted, based on simulated data, that the optimum distance for the application of the SFM with current HST instruments is approximately that of Virgo. The identification of background galaxies suffers in closer disks, as the stellar disk becomes more resolved, compounding confusion. This optimum distance, combined with the availability of deep HST/WFPC2 images from the Cepheid Extragalactic Distance Scale Key Project, resulted in the sample presented in Holwerda et al. (2005b). Holwerda et al. (2005d) confirmed the results from González et al. (2003) using this sample, with foreground disks spanning distances between 3.5 and 35 Mpc. A selection effect of the Key Project is that the majority of the HST science fields is concentrated on spiral arms and exclude the centers of the galaxies.

Here, we present average extinction values for the whole WFPC2 field-of-view, minimizing the uncertainties to the extent possible. In our initial papers, we did not apply an inclination correction to the optical depths because the correction depends strongly on the dust geometry (see the discussion in Holwerda et al. 2005b). However, in this paper we assume a simple dust model in §6. The appropriate inclination correction $\times \cos(i)$ has been applied to the points in Figures 4 and 5, and in Table 4. The uncertainties in the tables and figures reflect the 1-sigma confidence levels produced by the combination of the Poisson error and the cosmic variance of background galaxies.

3.2. SED optical depth estimate

The average disk optical depth is derived from the *Spitzer* observations. First, the surface brightnesses within the WF chips’ footprint are measured³ (see Figure 1). Second, these are converted into a dust surface density using an SED model. Third, this surface density is translated into an *I*-band optical depth.

All the IRAC and MIPS data are convolved to the poorest resolution of the 160 micron observations (see Table 1), and the pixel scale is set to 9”. This is done with the *gauss*, *wcsmap* and *geotran* tasks, under IRAF. Subsequently, the overall flux is measured in the WFPC2 field of view (Figure 1). Because the L-shaped aperture is a highly unusual one, the aperture correction remains uncertain, but not negligible, since the FWHM at 160 micron (40’0) is of the order of the aperture diameter ($3 \times 1’3 \times 1’3$ in an L-shape). Published aperture corrections for the IRAC instruments (Hora et al. 2004) overestimate the correction for extended objects (Jarrett 2005). Here we use the aperture corrections for extended sources from Jarrett (2005) for IRAC fluxes,⁴ and from Muzerolle et al. (2005) for the MIPS fluxes⁵ (see also Table 1). Table 2 gives the average surface brightnesses for the seven *Spitzer* channels in the field-of-view of the three WF chips of the WFPC2 array. The uncertainties are derived from the variance in the sky. Generally, the surface brightnesses agree with the results presented by Dale et al. (2005) for the entire disks.

The second step is to convert these surface brightnesses to a dust surface density. Initially, we fitted only the MIPS fluxes with two blackbodies and derived surface densities from these (Holwerda et al. 2006). However, a more rigorous treatment of the IR fluxes can be done with a SED model, such as the one presented in Li & Draine (2001). This model uses the physics of grain heating and reradiation, and a model distribution of grain sizes and types. The updated version from Draine & Li (2007) has been fit to the data, and the results are shown in Figure 2. The derived stellar and dust surface brightnesses, dust surface density, and mean temperature are presented in Table 3. Dust surface densities are between 0.1 and $1.4 \times 10^6 M_{\odot} \text{ kpc}^{-2}$, with mean temperatures between 14.6 and 17.8 K.

The mean dust temperatures are obtained from the mean radiation scaling, \bar{U} ,⁶ in the Draine & Li (2007) model (T_2 in their equation 18). The model uses a distribution

³ The PC part of the WFPC2 array is not used in either analysis.

⁴<http://spider.ipac.caltech.edu/staff/jarrett/irac/calibration/index.html>

⁵<http://ssc.spitzer.caltech.edu/mips/apercorr/>

⁶The Draine & Li (2007) model uses a distribution of scaling values (U) of the local Interstellar Radiation Field to calculate the irradiation that the grains see. \bar{U} is the average of this scaling distribution.

of temperatures and grain sizes. Therefore the mean temperature is an indication of the thermal equilibrium point of the bulk of the dust. Most of the dust is cold ($T < 25$ K).

These results are an obvious improvement over a simple single-temperature fit, but the model parameters in Table 3 are still not fully constrained; disagreement between data and model at the PAH peak at 8 micron could be an effect of metallicity or the presence of a bright HII region. The 70 and 160 μ m fluxes hint at colder or more dust in the disk (Figure 2). There are three caveats to the fits: (1) a lack of sub-mm data, (2) the single color ISRF used and (3) averaging over different types of emission regions, i.e., HII regions and the general disk.

Additional sub-mm data of comparable quality, needed to better constrain the model and especially the cold dust emission, will not be available until SCUBA2 starts operations on the JCMT and the launch of *Herschel*.⁷ At present, comparable-quality sub-mm maps are available only for NGC 5194 (Meijerink et al. 2005) and NGC 7331 (Regan et al. 2004). Draine et al. (2007) discuss SED models with and without sub-mm data.

The second caveat in the derivation of dust mass is the assumption of a constant color for the interstellar radiation field (ISRF) illuminating the emitting dust. In reality, dust grains deeper in a dust structure will encounter radiation field that is not only dimmed but also reddened and, hence, will contribute less flux to the FIR emission. Locally, the ISRF will also depend on the age of the nearby stellar population. Due to the reddening of the ISRF deeper in the cloud, dense clouds could contain more dust mass in their centers than inferred from just the FIR emission. Additional sub-mm observations will help resolve this uncertainty in the SED optical depth. Draine et al. (2007) discuss fits of the model to the total fluxes of the SINGS galaxies with and without additional sub-mm data. They find that the FIR estimate underestimates of 1.5 times the dust mass more (5 out of 17 cases, notably NGC 3627 and 7331 of our sample) than overestimates it (only M51 of the 17).

The third caveat is that the model values are an average over many different types of ISM regions, each with a different heating mechanism, dust structure and composition (e.g., photo-dissociation regions, cirrus, and star-forming regions in spiral arms). The Draine & Li (2007) model’s assumptions hold better for some regions than for others, but we use the results as “typical” for these disks. The relative contribution of PAH emission to the SED is a function of ISM geometry as well as irradiation and composition (e.g., Silva et al. 1998; Piovan et al. 2006). Together with a better-constrained FIR/sub-mm SED one could constrain ISM geometry solely from the relative contributions to the SED. Draine et al.

⁷*Herschel* data will be especially valuable as it will not suffer from night sky structure, which is of similar angular size as these disks.

(2007) discuss the application of the Draine & Li (2007) model to whole disks of the SINGS galaxies.

The dust surface density is translated into an average optical depth with the absorption cross section per unit dust mass, $\kappa_{abs}(\lambda)$, and grain albedo from Draine (2003) for the Johnson *I*-band (865.5 Å): $\tau_m = \kappa_{abs} \times (1 - Albedo) \times M_{dust}/area$. These optical depth values are presented in Table 4.

4. Cloud size and the SFM

It continues to be difficult to constrain dusty cloud geometry from models of either extinction or emission. In this section, we review what can be learned, solely from the SFM measurements, about the geometry of the extinguishing medium.

In Holwerda et al. (2005b), two indications that the dust disk is clumpy are identified: (1) the average color of the distant galaxies is independent of the disk opacity implied by their number, and (2) the measurement of disk opacity is independent of inclination. The lack of a relation between the average opacity of the disk and the average color of the detected galaxies can be explained by two scenarios: (1) some of the background galaxies are completely blocked by large clouds, and some are not. The color measurement is done on background objects that do not suffer from extinction and, hence, reddening. Alternatively, (2) *all* background galaxies are dimmed by clouds smaller than the projected distant galaxies. Consequently, some of the distant galaxies are dimmed enough to drop below the detection threshold. Any detected galaxy’s color is, however, measured from mostly unreddened flux.⁸ However, we note that a relation between the reddening and derived extinction from the distant galaxies is difficult to detect because (1) the spread in colors of distant galaxies is substantial and (2) color is measured from the detected galaxies –automatically the least dimmed– whereas opacity is measured from the *missing* galaxies.

The inclination effect on the apparent optical depth from the number of distant galaxies is minimal (see Holwerda et al. 2005b, §5.1 and Figure 3). Assuming a thin layer of optically thick clouds, the apparent optical depth of the disk, measured from the number of distant galaxies, is dominated by the apparent filling factor of clouds. The projected filling factor

⁸The effect of cloud geometry on the luminosity function of the detected distant galaxies is, in principle, another possible way to distinguish between cloud geometries, but this is complicated by the fact that the detection limit of distant galaxies is dominated by the field properties (brightness and granularity), rather than by the dimming by the dust. See also the discussions in Holwerda et al. (2005d), and Appendix B in Holwerda (2005).

does not change much with inclination: a flat cloud covering 40% of a certain disk section still covers 40% of the inclined section. Only when the height of the cloud becomes important –when the inclination is closer to edge-on–, does the apparent filling factor change. This explanation for the lack of an inclination effect in the opacity profiles does not depend on the size of the clouds. It could be a single, large, cloud or many small ones in the plane of the disk. However, the optical depth values in Holwerda et al. (2005b) are from different sections of the disks –although generally centered on a spiral arm– and the effect of small inclination differences could well have been masked by comparing different regions in the disks. In Holwerda et al. (2005b) we did not apply an inclination correction because it depends on the assumed dust geometry. In this paper we do assume a dust geometry and hence make an inclination correction (§6).

The simulations in the SFM assume a gray screen, an uniform unclumped dust layer with opacity equal in the V and I bands. The SFM opacity measurements in this paper are based on such simulations. In Holwerda (2005), we ran a series of simulations on NGC 1365⁹ to characterize the effect of average cloud cross-section on the number of distant galaxies observable through a disk.

Figure 3 shows the effect of cloud size, expressed in pixels, on the simulated relation between average opacity and number of distant objects. In each simulation, we fix a cloud size and vary their number to increase disk opacity. An ensemble of unresolved clouds is effectively the gray screen. For clouds resolved with HST, more than 2 pixels¹⁰, the relation between opacity (cloud filling factor) and number of distant objects becomes much shallower. The same number of distant galaxies observed would then imply a much *higher* opacity of the disk. Because the SFM (calibrated with a gray screen) generally agrees well with measurements from overlapping galaxies (Holwerda et al. 2005b), it seems unlikely that the disk’s opacity is predominantly due to large, resolved clouds. A pixel of 0'05 at the distance of NGC 1365 (18 Mpc) is 4 pc in linear size. It is therefore implied that the structure of the ISM responsible for the disk opacity measured with the SFM varies in optical depth on scales of ~ 10 pc or less.

From the SFM measurements alone, the cloud geometry is impossible to determine. Only when additional information is used –e.g., the general agreement with the occulting galaxy technique– it favors small (unresolved) scales for the clouds. Therefore, to constrain cloud geometry, information from two different techniques needs to be combined.

⁹NGC 1365 is one of the more distant galaxies in the Holwerda et al. (2005b) sample, and we ran these simulations as a validation of the gray screen synthetic fields.

¹⁰Pixel scale is 0'05 in our data, after the drizzle reduction.

5. Optical depths

Table 4 presents the optical depth estimates from the Synthetic Field Method and the SED model (Draine 2003; Draine & Li 2007), for the WFPC2 field-of-view. The optical depths range between 0.1 and 3.5 magnitudes in the I -band. The measurements are for different parts of different spiral disks (Figure 1), explaining in part the range in values.

The optical depth estimates presented here may appear high for the Johnson I -band, compared with other extinction estimates (e.g., those from inclination effects or reddening), but these are (1) for the entire height of the disk, and (2) generally centered on a spiral arm. Typical extinction values in the I -band are several tenths of a magnitude for a dust screen in front of the stellar spiral disk (e.g., Meyer et al. 2006). Two of the derived SFM opacities are negative, possibly the effect of an overdensity of distant galaxies behind the target galaxy. The discrepancy in NGC5194-1 may be due to misidentification of background galaxies, as they are difficult to identify in this field.

Figures 4 and 5 show the values of disk opacity by both methods, over the same section of the disk. Both methods generally agree within the uncertainties of the measurements. The agreement is better than our initial estimate from a blackbody fit to the MIPS fluxes in Holwerda et al. (2006). The general agreement and the mean temperature of the dust (Table 3) imply that most of a disk’s opacity is due to the cold dust in the disk.

6. Model of cloud geometry

The relation between the apparent and average I -band optical depth measurements –the first from the number of distant galaxies in HST images and the second derived from the *Spitzer* SED– could reveal the nature of the prevalent structure in the ISM.

The *a priori* assumptions are that (1) all dust structure is transparent to the FIR emission from which the dust surface density is estimated in the SED model, and (2) the *entire* volume of the cloud emits in the FIR. We adopt *Model C* from Natta & Panagia (1984), in which a randomly distributed series of clumps covers the area. These authors define two optical depths: (1) the typical optical depth (τ_m), i.e., the average optical depth that is proportional to the dust mass; and (2) the apparent optical depth ($\tilde{\tau}$), or the optical depth if a uniform layer would cover the area.

Our two measurements of optical depth –SED and SFM– correspond to these two optical depths, average and apparent. An optical depth based on the SED depends on the dust mass within the area, and hence corresponds to τ_m . The SFM optical depth is the apparent optical

depth averaged over the area, and hence $\tilde{\tau}$. These two optical depths need not be the same, and their relation is an indication of how clumped the medium is.

Let us assume a number of small dust structures with a height (h), an average grain cross-section (σ), and a grain emissivity (Q). The grain number density in the clouds is denoted by n_d , and the average number of clouds in a line-of-sight is n . We assume all clumps have the same optical depth τ_c :

$$\tau_c = h n_d \sigma Q. \quad (1)$$

The average optical depth (τ_m) is then:

$$\tau_m = n \times \tau_c, \quad (2)$$

and the apparent optical depth can be derived if one assumes a Gaussian distribution of the number of clouds along the possible lines-of-sight and sum the contributions of all clouds (see equations 15 and 17-19 in Natta & Panagia 1984):

$$\tilde{\tau} = n \times (1 - e^{-\tau_c}), \quad (3)$$

with asymptotic values for both optically thin and thick clouds:

$$\tau_c \rightarrow 0, \Rightarrow \tau_m \rightarrow 0, \tilde{\tau} \rightarrow \tau_m, \quad (4)$$

$$\tau_c \rightarrow \infty, \Rightarrow \tau_m \rightarrow \infty, \tilde{\tau} \rightarrow n. \quad (5)$$

We note that the inferred dust mass in the disk (M_{dust}) is proportional to the number of clouds (n) and the cloud optical depth (τ_c). The ratio of the apparent over the average optical depth is:

$$\frac{\tilde{\tau}}{\tau_m} = \frac{1 - e^{-\tau_c}}{\tau_c}, \quad (6)$$

leaving only the optical depth of the clouds (τ_c), and hence the grain density (n_d) and the cloud size (h) as the variables. Our fit to the relation between SFM and SED optical depth estimates only has τ_c as the variable (Figure 4).

We can now use equation 6 to derive τ_c from a fit to the optical depths from SED (τ_m), and from the number of distant galaxies ($\tilde{\tau}$). We want to answer three questions. Are the clouds in the disks typically optically thin or thick? If all disks are equal, what is the implied cloud optical depth? How many clouds lie typically along a given line-of-sight?

6.1. Optically thick or thin clouds?

Optically thin clouds ($\tau_c \ll 1$) result in a ratio of optical depths close to unity:

$$\frac{\tilde{\tau}}{\tau_m} = \frac{1 - e^{-\tau_c}}{\tau_c} \approx \frac{1 - (1 - \tau_c)}{\tau_c} = 1; \quad (7)$$

optically thick clouds ($\tau_c \gg 1$) result in a ratio of:

$$\frac{\tilde{\tau}}{\tau_m} = \frac{1 - e^{-\tau_c}}{\tau_c} < 1. \quad (8)$$

Figures 4 and 5 show how a majority of the data exhibit a ratio of order unity. The cold dust mass in the SED model could be better constrained with additional sub-mm information (Draine et al. 2007). However, the ratios are, within the errors, consistent with optically thin clouds in most of the disks.

6.2. Cloud size

Figure 4 shows the fit to the ratios of apparent to average optical depths, with τ_c as the single fit parameter, as per equation 6. For simplicity, we assume here that all disks are made up of similar clouds, and that there is no difference between arm and disk regions. The negative SFM measurements are excluded from the fit. The best fit is for a cloud optical depth of $\tau_c = 0.4$ with, on average, 2.6 clouds along the line-of-sight (if the two negative points are included, the values change, respectively, to $\tau_c = 0.56$ and $n = 1.9$). The inferred value of τ_c is likely to be a mean between higher values in spiral arms and much lower values in the disk. Optically thick disks have more clouds along the line of sight, while optically thin disks harbor a single cloud.

Reasonable values for the parameters in equation 1 are: $n_d \approx 5 \times 10^{-3}$ grains m^{-3} ,

$\sigma = 0.03 \mu\text{m}^2$ and $Q = \frac{3}{1300} \left(\frac{125}{160}\right)^\beta = 1.5 \times 10^{-3}$ with $\beta = 2$ (Hildebrand 1983)¹¹. The value of 0.4 for τ_c implies a cloud height, h , of ~ 60 pc! Much larger clouds could be resolved in extinction maps of these disks based on stellar reddening. In the case of NGC 3627, NGC 5194, NGC 6946 and NGC 7331, there is a clear spiral arm in the reddening map (Meyer et al. 2006; Holwerda et al. 2007); the other reddening maps are smooth or do not extend out to cover the whole WFPC2 pointing.

A more likely scenario is that there is an inverse relation between the cloud density n_d and scale h . Such a relation can be seen in giant molecular clouds (GMC) of our own Galaxy (e.g. Solomon et al. 1987). In this case, the single optically thin cloud can be replaced by smaller optically thick ones. We note that the largest GMCs are of the order of 60 pc.

The value of 60 pc clouds appears in contradiction to the implied size in the SFM calibration (~ 10 pc). However, the typical cloud size can be 60 pc and still the disk opacity can change over smaller scales, if several partially overlapping clouds are seen in projection. The inverse relation between scale and density would also help make the two scales compatible.

Our data are consistent with optically thin clouds ($\tau_c = 0.4$) and their average opacity value implies a typical cloud size that is unresolved with *Spitzer* in our galaxies.

6.3. Cloud Numbers

The above fit to the relation between $\tilde{\tau}$ and τ_m indicates that, on average, more than one cloud is needed along the line-of-sight in most disks ($\bar{n} = 2.6$). However, the assumption was that τ_c had a single value for all the disks. In §6.1, we argued that the ratio between $\tilde{\tau}$ and τ_m implied the τ_c is optically thin. It logically follows that optically thick disks must have more than a single cloud along the line-of-sight.

Figure 5 illustrates the effect of number of clouds along the line-of-sight (n) on the relation between $\tilde{\tau}$ and τ_m , when τ_c is freely increased from 0 to τ_m/n (the lines have been drawn according to equations 2 and 3). We note that all disks are consistent with many clouds along the line-of-sight –including the optically thin ones, also because they lie in the optically thin cloud ($\tilde{\tau}/\tau_m \sim 1$, $\tau_c < 1$) regime.

¹¹There is substantial discussion in the literature about the value of β (e.g., Bendo et al. 2003). β was fixed at 2 in the Draine & Li (2007) models.

6.4. Potential Improvements

There are many refinements to be made to the simple model presented here. Some improvements for future comparisons between these two measurements of optical depth are: (1) a distribution of cloud sizes for both the SFM calibration, as well as in the model explaining the ratio between SFM and SED optical depths. A model distribution can be taken from observations of GMCs in our own Galaxy and nearby ones (Heyer et al. 2001; Rosolowsky 2005). The cross-section distribution could be used in SFM measurements in the future. A cross-section distribution can only be applied, if the foreground disk is at a single, fixed distance; only one counts though a single foreground galaxy are used. There are three face-on spirals with enough solid angle in HST imaging as well as additional *Spitzer* data: M51, M81 and M101. (2) The SED model can be much better constrained with additional sub-mm observations, the opportunities for which will expand dramatically in the near future (*SCUBA2* on the JCMT and *Herschel* satellite). (3) The effects of grand design spiral arms and galactic radius could be identified in a single disk; the comparison SFM and SED is not made for different sections of the disks combined. (4) A future SED model can take into account the reddening of the interstellar radiation field, as it penetrates the ISM. This would require a comprehensive treatment of the ISM structure in addition to its temperature, composition and irradiation.

7. Conclusions

To constrain models of the spiral disk’s energy budget with typical values for the size of dusty clouds in the ISM, we compare two techniques to extract the average and apparent optical depths of a section of spiral disk. From the comparison between SFM and SED results, we conclude the following:

1. The SFM’s calibration alone implies projected cloud scales predominantly unresolved with HST (of the order of 10 pc in NGC 1365, see §4 and Figure 3).
2. The dust responsible for the disk’s opacity is predominantly cold ($T < 25$ K, Table 3).
3. The average and apparent optical depths of these disk sections, measured from SED and SFM respectively, generally agree (Figure 4 and 5). This implies generally optically thin clouds ($\tau_c < 1$, §6.1).
4. The fit to the ratio between apparent and average optical depth measurements, $\tilde{\tau}/\tau_m$, indicates a cloud optical depth, τ_c , of 0.4, more than a single cloud along the line-of-sight, and a cloud size of ~ 60 pc. If several partially overlapping clouds are seen in

projection through the disk, the disk’s opacity will change over smaller scales, consistent with conclusion 1.

6. Optically thick disks appear to have more than a single cloud along the line-of-sight (Figure 5) and optically thin disks may have several clouds as well.

Future work using counts of distant galaxies through a foreground disk could be used to find cold dust structures at larger galactic radii, provided a sufficiently large solid angle has been imaged with HST/ACS’s superb resolution.¹² Notably, the ACS data on M51, M81 and M101 are very promising for such an analysis.¹³ *Spitzer* observations of these nearby disks are also available, making a similar comparison between SED and apparent optical depth possible for portions of these disks. The typical cloud scale for spiral arms or disk sections or as a function of galactic radius could then be found. The SCUBA-2 instrument has recently been installed on the James Clerk Maxwell Telescope. A project with SCUBA-2 to map the SINGS galaxies in two sub-mm bands will improve future SED modelling of these spiral disks significantly over the SED models presented here.

This work is based in part on archival data obtained with the *Spitzer* Space Telescope, which is operated by JPL, CalTech, under a contract with NASA. This work is also based on observations with the NASA/ESA Hubble Space Telescope, obtained at the STScI, which is operated by the Association of Universities for Research in Astronomy (AURA), Inc., under NASA contract NAS5-26555.

The authors would like to thank T. Jarrett, for making his aperture corrections of extended sources available to us at an early stage, and Erik Rosolowsky, for useful discussions on Local Group cloud sizes. We would like to thank Maarten Baes for discussion of the motivation. We would also like to thank George Bendo, Erik Hollenback and Kristen Keener for their comments on earlier drafts of this paper.

REFERENCES

Alton, P. B., Bianchi, S., Rand, R. J., Xilouris, E. M., Davies, J. I., & Trewhella, M. 1998, *ApJ*, 507, L125

¹²See Holwerda et al. (2005d) for selection criteria of suitable data.

¹³The closer disks are slightly less well suited for the SFM because their stellar disk is resolved, but the loss in accuracy is offset by the larger available solid angle.

- Alton, P. B., Xilouris, E. M., Misiriotis, A., Dasyra, K. M., & Dumke, M. 2004, *A&A*, 425, 109
- Andredakis, Y. C. & van der Kruit, P. C. 1992, *A&A*, 265, 396
- Bendo, G. J., Dale, D. A., Draine, B. T., Engelbracht, C. W., Kennicutt, Jr., R. C., Calzetti, D., Gordon, K. D., Helou, G., Hollenbach, D., Li, A., Murphy, E. J., Prescott, M. K. M., & Smith, J.-D. T. 2006, *ApJ*
- Bendo, G. J., Joseph, R. D., Wells, M., Gallais, P., Haas, M., Heras, A. M., Klaas, U., Laureijs, R. J., Leech, K., Lemke, D., Metcalfe, L., Rowan-Robinson, M., Schulz, B., & Telesco, C. 2003, *AJ*, 125, 2361
- Berlind, A. A., Quillen, A. C., Pogge, R. W., & Sellgren, K. 1997, *AJ*, 114, 107
- Bianchi, S. 2007, *ArXiv e-prints*, 705
- Bianchi, S., Davies, J. I., & Alton, P. B. 2000a, *A&A*, 359, 65
- Bianchi, S., Ferrara, A., Davies, J. I., & Alton, P. B. 2000b, *MNRAS*, 311, 601
- Boissier, S., Boselli, A., Buat, V., Donas, J., & Milliard, B. 2004, *A&A*, 424, 465
- Calzetti, D., Kennicutt, R. C., Bianchi, L., Thilker, D. A., Dale, D. A., Engelbracht, C. W., Leitherer, C., Meyer, M. J., Sosey, M. L., Mutchler, M., Regan, M. W., Thornley, M. D., Armus, L., Bendo, G. J., Boissier, S., Boselli, A., Draine, B. T., Gordon, K. D., Helou, G., Hollenbach, D. J., Kewley, L., Madore, B. F., Martin, D. C., Murphy, E. J., Rieke, G. H., Rieke, M. J., Roussel, H., Sheth, K., Smith, J. D., Walter, F., White, B. A., Yi, S., Scoville, N. Z., Polletta, M., & Lindler, D. 2005, *ApJ*, 633, 871
- Dale, D. A., Bendo, G. J., Engelbracht, C. W., Gordon, K. D., Regan, M. W., Armus, L., Cannon, J. M., Calzetti, D., Draine, B. T., Helou, G., Joseph, R. D., Kennicutt, R. C., Li, A., Murphy, E. J., Roussel, H., Walter, F., Hanson, H. M., Hollenbach, D. J., Jarrett, T. H., Kewley, L. J., Lamanna, C. A., Leitherer, C., Meyer, M. J., Rieke, G. H., Rieke, M. J., Sheth, K., Smith, J. D. T., & Thornley, M. D. 2005, *ApJ*, 633, 857
- Dale, D. A., de Paz, A. G., Gordon, K. D., Hanson, H. M., Armus, L., Bendo, G. J., Bianchi, L., Block, M., Boissier, S., Boselli, A., Buckalew, B. A., Buat, V., Burgarella, D., Calzetti, D., Cannon, J. M., Engelbracht, C. W., Helou, G., Hollenbach, D. J., Jarrett, T. H., Kennicutt, R. C., Leitherer, C., Li, A., Madore, B. F., Martin, D. C., Meyer, M. J., Murphy, E. J., Regan, M. W., Roussel, H., Smith, J. D. T., Sosey, M. L., Thilker, D. A., & Walter, F. 2007, *ApJ*, 655, 863

- Dasyra, K. M., Xilouris, E. M., Misiriotis, A., & Kylafis, N. D. 2005, *A&A*, 437, 447
- Davies, J. I., Alton, P., Trewhella, M., Evans, R., & Bianchi, S. 1999, *MNRAS*, 304, 495
- Domingue, D. L., Keel, W. C., Ryder, S. D., & White, R. E. 1999, *AJ*, 118, 1542
- Domingue, D. L., Keel, W. C., & White, R. E. 2000, *ApJ*, 545, 171
- Dopita, M. A., Fischera, J., Sutherland, R. S., Kewley, L. J., Leitherer, C., Tuffs, R. J., Popescu, C. C., van Breugel, W., & Groves, B. A. 2006a, *ApJS*, 167, 177
- Dopita, M. A., Fischera, J., Sutherland, R. S., Kewley, L. J., Tuffs, R. J., Popescu, C. C., van Breugel, W., Groves, B. A., & Leitherer, C. 2006b, *ApJ*, 647, 244
- Draine, B. T. 2003, *ARA&A*, 41, 241
- Draine, B. T., Dale, D. A., Bendo, G., Gordon, K. D., Smith, J. D. T., Armus, L., Engelbracht, C. W., Helou, G., Kennicutt, Jr., R. C., Li, A., Roussel, H., Walter, F., Calzetti, D., Moustakas, J., Murphy, E. J., Rieke, G. H., Bot, C., Hollenbach, D. J., Sheth, K., & Teplitz, H. I. 2007, *ApJ*, 663, 866
- Draine, B. T. & Li, A. 2007, *ApJ*, 657, 810
- Driver, S. P., Popescu, C. C., Tuffs, R. J., Liske, J., Graham, A. W., Allen, P. D., & De Propris, R. 2007, *ArXiv e-prints*, 704
- Elmegreen, D. M., Kaufman, M., Elmegreen, B. G., Brinks, E., Struck, C., Klarić, M., & Thomasson, M. 2001, *AJ*, 121, 182
- Engelbracht, C. W., Gordon, K. D., Bendo, G. J., Pérez-González, P. G., Misselt, K. A., Rieke, G. H., Young, E. T., Hines, D. C., Kelly, D. M., Stansberry, J. A., Papovich, C., Morrison, J. E., Egami, E., Su, K. Y. L., Muzerolle, J., Dole, H., Alonso-Herrero, A., Hinz, J. L., Smith, P. S., Latter, W. B., Noriega-Crespo, A., Padgett, D. L., Rho, J., Frayer, D. T., & Wachter, S. 2004, *ApJS*, 154, 248
- Engelbracht, C. W., Kundurthy, P., Gordon, K. D., Rieke, G. H., Kennicutt, R. C., Smith, J.-D. T., Regan, M. W., Makovoz, D., Sosey, M., Draine, B. T., Helou, G., Armus, L., Calzetti, D., Meyer, M., Bendo, G. J., Walter, F., Hollenbach, D., Cannon, J. M., Murphy, E. J., Dale, D. A., Buckalew, B. A., & Sheth, K. 2006, *ApJ*, 642, L127
- Genzel, R. & Cesarsky, C. J. 2000, *ARA&A*, 38, 761
- González, R. A., Allen, R. J., Dirsch, B., Ferguson, H. C., Calzetti, D., & Panagia, N. 1998, *ApJ*, 506, 152

- González, R. A., Loinard, L., Allen, R. J., & Muller, S. 2003, *AJ*, 125, 1182
- Gordon, K. D., Bailin, J., Engelbracht, C. W., Rieke, G. H., Misselt, K. A., Latter, W. B., Young, E. T., Ashby, M. L. N., Barmby, P., Gibson, B. K., Hines, D. C., Hinz, J., Krause, O., Levine, D. A., Marleau, F. R., Noriega-Crespo, A., Stolovy, S., Thilker, D. A., & Werner, M. W. 2006, *ApJ*, 638, L87
- Gordon, K. D., Pérez-González, P. G., Misselt, K. A., Murphy, E. J., Bendo, G. J., Walter, F., Thornley, M. D., Kennicutt, Jr., R. C., Rieke, G. H., Engelbracht, C. W., Smith, J.-D. T., Alonso-Herrero, A., Appleton, P. N., Calzetti, D., Dale, D. A., Draine, B. T., Frayer, D. T., Helou, G., Hinz, J. L., Hines, D. C., Kelly, D. M., Morrison, J. E., Muzerolle, J., Regan, M. W., Stansberry, J. A., Stolovy, S. R., Storrie-Lombardi, L. J., Su, K. Y. L., & Young, E. T. 2004, *ApJS*, 154, 215
- Gordon, K. D., Rieke, G. H., Engelbracht, C. W., Muzerolle, J., Stansberry, J. A., Misselt, K. A., Morrison, J. E., Cadien, J., Young, E. T., Dole, H., Kelly, D. M., Alonso-Herrero, A., Egami, E., Su, K. Y. L., Papovich, C., Smith, P. S., Hines, D. C., Rieke, M. J., Blaylock, M., Pérez-González, P. G., Le Floc'h, E., Hinz, J. L., Latter, W. B., Hesselroth, T., Frayer, D. T., Noriega-Crespo, A., Masci, F. J., Padgett, D. L., Smylie, M. P., & Haegel, N. M. 2005, *PASP*, 117, 503
- Heyer, M. H., Carpenter, J. M., & Snell, R. L. 2001, *ApJ*, 551, 852
- Hildebrand, R. H. 1983, *QJRAS*, 24, 267
- Hinz, J. L., Misselt, K., Rieke, M. J., Rieke, G. H., Smith, P. S., Blaylock, M., & Gordon, K. D. 2006, *ApJ*, 651, 874
- Hodge, P. W. 1974, *ApJ*, 192, 21
- Holwerda, B. W. 2005, PhD thesis, Kapteyn Astronomical Institute
- Holwerda, B. W., González, R. A., Allen, R. J., & van der Kruit, P. C. 2005a, *AJ*, 129, 1381
- . 2005b, *AJ*, 129, 1396
- . 2005c, *A&A*, 444, 101
- . 2005d, *A&A*, 444, 319
- Holwerda, B. W., González, R. A., Calzetti, D., Allen, R. J., van der Kruit, P. C., & the SINGS team. 2006, arXiv:astro-ph/0603395

- Holwerda, B. W., González, R. A., van der Kruit, P. C., & Allen, R. J. 2005e, *A&A*, 444, 109
- Holwerda, B. W., Meyer, M., Regan, M., Calzetti, D., Gordon, K. D., Smith, J. D., Dale, K., Engelbracht, C. W., Jarrett, T., Thornley, M. D., Bot, C., Buckalew, B. A., Kennicutt, R. C., & González, R. A. 2007, *AJ*, *submitted*
- Hora, J. L., Fazio, G. G., Allen, L. E., Ashby, M. L. N., Barmby, P., Deutsch, L. K., Huang, J. S., Marengo, M., Megeath, S. T., Melnick, G. J., Pahre, M. A., Patten, B. M., Smith, H. A., Wang, Z., Willner, S. P., Hoffmann, W. F., Pipher, J. L., Forrest, W. J., McMurtry, C. W., McCreight, C. R., McKelvey, M. E., McMurray, Jr., R. E., Moseley, S. H., Arendt, R. G., Mentzell, J. E., Marx, C. T., Fixsen, D. J., Tollestrup, E. V., Eisenhardt, P. R., Stern, D., Gorjian, V., Bhattacharya, B., Carey, S. J., Glaccum, W. J., Lacy, M. D., Lowrance, P. J., Laine, S. J., Nelson, B. O., Reach, W. T., Stauffer, J. R., Surace, J. A., Wilson, G., & Wright, E. L. 2004, in *Microwave and Terahertz Photonics*. Edited by Stohr, Andreas; Jager, Dieter; Iezekiel, Stavros. *Proceedings of the SPIE*, Volume 5487, pp. 77-92 (2004)., ed. J. C. Mather, 77–92
- Jarrett, J. 2005, *IRAC: Extended Source Calibration*
- Kamphuis, P., Holwerda, B. W., Allen, R. J., Peletier, R. F., & van der Kruit, P. C. 2007, *ArXiv e-prints/0706.2275*
- Keel, W. C. & White, R. E. 2001a, *AJ*, 121, 1442
- . 2001b, *AJ*, 122, 1369
- Kennicutt, R. C., Armus, L., Bendo, G., Calzetti, D., Dale, D. A., Draine, B. T., Engelbracht, C. W., Gordon, K. D., Grauer, A. D., Helou, G., Hollenbach, D. J., Jarrett, T. H., Kewley, L. J., Leitherer, C., Li, A., Malhotra, S., Regan, M. W., Rieke, G. H., Rieke, M. J., Roussel, H., Smith, J. T., Thornley, M. D., & Walter, F. 2003, *PASP*, 115, 928
- Li, A. & Draine, B. T. 2001, *ApJ*, 554, 778
- MacGillivray, H. T. 1975, *MNRAS*, 170, 241
- Meijerink, R., Tilanus, R. P. J., Dullemond, C. P., Israel, F. P., & van der Werf, P. P. 2005, *A&A*, 430, 427
- Meyer, M., Calzetti, D., & Regan, M. 2006, *ApJ*, 1, 1
- Misiriotis, A. & Bianchi, S. 2002, *A&A*, 384, 866

- Misiriotis, A., Popescu, C. C., Tuffs, R., & Kylafis, N. D. 2001, *A&A*, 372, 775
- Muzerolle, J., Gordon, K., Engelbracht, C., & Stansberry, J. 2005, MIPS aperture corrections
- Natta, A. & Panagia, N. 1984, *ApJ*, 287, 228
- Nelson, A. E., Zaritsky, D., & Cutri, R. M. 1998, *AJ*, 115, 2273
- Pérez-González, P. G., Kennicutt, Jr., R. C., Gordon, K. D., Misselt, K. A., Gil de Paz, A., Engelbracht, C. W., Rieke, G. H., Bendo, G. J., Bianchi, L., Boissier, S., Calzetti, D., Dale, D. A., Draine, B. T., Jarrett, T. H., Hollenbach, D., & Prescott, M. K. M. 2006, *ApJ*, 648, 987
- Piovan, L., Tantalò, R., & Chiosi, C. 2006, *MNRAS*, 366, 923
- Popescu, C. C., Misiriotis, A., Kylafis, N. D., Tuffs, R. J., & Fischera, J. 2000, *A&A*, 362, 138
- Popescu, C. C. & Tuffs, R. J. 2003, *A&A*, 410, L21
- Popescu, C. C. & Tuffs, R. J. 2005, in *AIP Conf. Proc. 761: The Spectral Energy Distributions of Gas-Rich Galaxies: Confronting Models with Data*, 155–+
- Radovich, M., Kahanpää, J., & Lemke, D. 2001, *A&A*, 377, 73
- Regan, M. W., Thornley, M. D., Bendo, G. J., Draine, B. T., Li, A., Dale, D. A., Engelbracht, C. W., Kennicutt, R. C., Armus, L., Calzetti, D., Gordon, K. D., Helou, G., Hollenbach, D. J., Jarrett, T. H., Kewley, L. J., Leitherer, C., Malhotra, S., Meyer, M., Misselt, K. A., Morrison, J. E., Murphy, E. J., Muzerolle, J., Rieke, G. H., Rieke, M. J., Roussel, H., Smith, J.-D. T., & Walter, F. 2004, *ApJS*, 154, 204
- Rosolowsky, E. 2005, *PASP*, 117, 1403
- Seth, A. C., Dalcanton, J. J., & de Jong, R. S. 2005, *AJ*, 130, 1574
- Shapley, H. 1951, *Proceedings of the National Academy of Science*, 37, 133
- Silva, L., Granato, G. L., Bressan, A., & Danese, L. 1998, *ApJ*, 509, 103
- SINGS team. 2006, SINGS fourth data delivery release notes, SINGS team
- Solomon, P. M., Rivolo, A. R., Barrett, J., & Yahil, A. 1987, *ApJ*, 319, 730
- Thornley, M. D., Braine, J., & Gardan, E. 2006, *ApJ*, 651, L101

- Trewhella, M., Davies, J. I., Alton, P. B., Bianchi, S., & Madore, B. F. 2000, *ApJ*, 543, 153
- Tuffs, R. J. & Popescu, C. C. 2005, in *AIP Conf. Proc. 761: The Spectral Energy Distributions of Gas-Rich Galaxies: Confronting Models with Data*, 344–+
- Tuffs, R. J., Popescu, C. C., Völk, H. J., Kylafis, N. D., & Dopita, M. A. 2004, *A&A*, 419, 821
- Wesselink, A. J. 1961, *MNRAS*, 122, 509
- White, R. E. & Keel, W. C. 1992, *Nature*, 359, 129
- White, R. E., Keel, W. C., & Conselice, C. J. 2000, *ApJ*, 542, 761
- Witt, A. N. & Gordon, K. D. 2000, *ApJ*, 528, 799
- Xilouris, E. M., Byun, Y. I., Kylafis, N. D., Paleologou, E. V., & Papamastorakis, J. 1999, *A&A*, 344, 868

.
. .
. .
. .

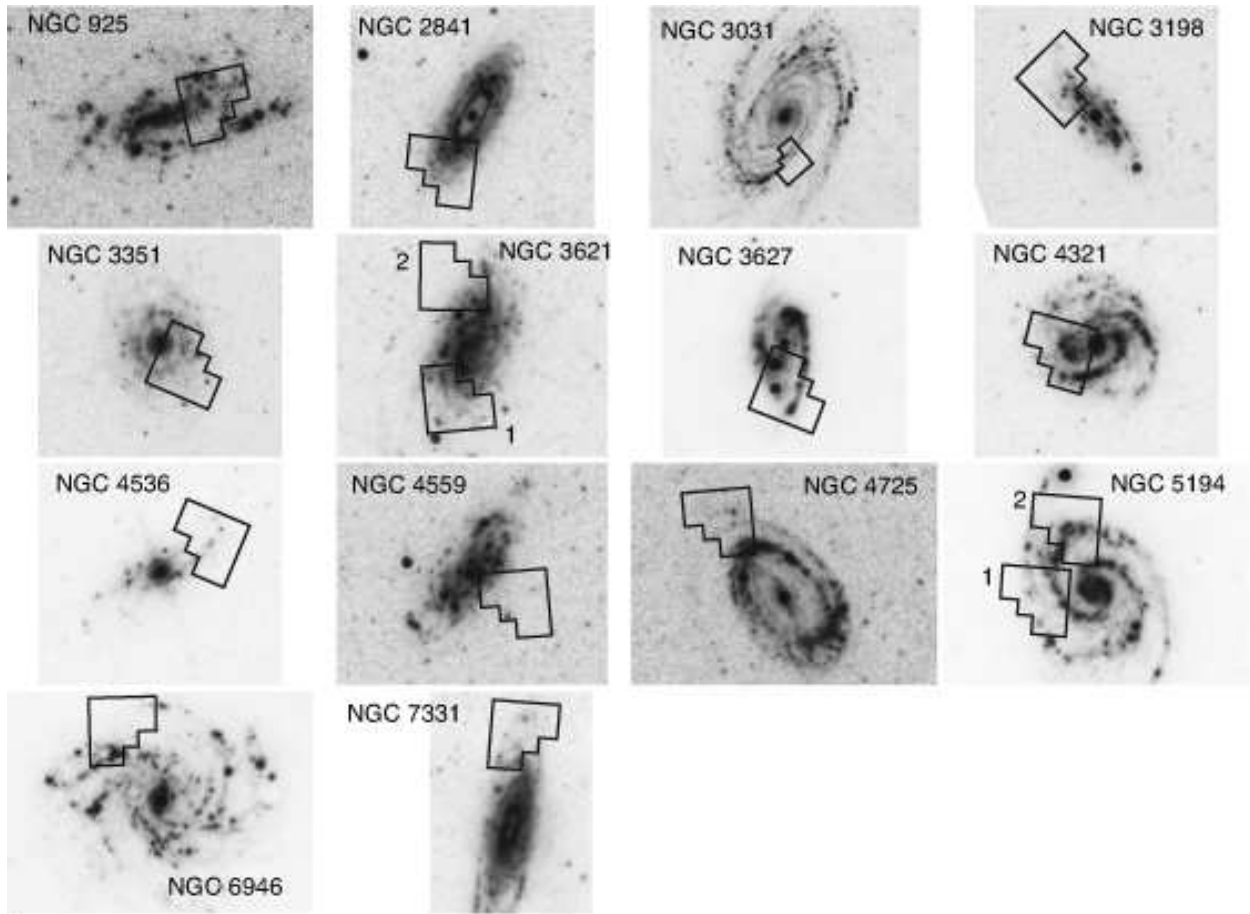


Fig. 1.— The footprints of the WFC2 camera on board HST, on the 24 micron images from the MIPS detector onboard *Spitzer*. Most of the HST images do not include the center, and are pointed on a spiral arm. NGC 3621 and NGC 5195 (M51) have two separate WFC2 fields associated with them. The PC chip, i.e, the small chip in the nook of the “L” of the three WF chips, is not used for the SFM analysis, nor as part of our *Spitzer* aperture.

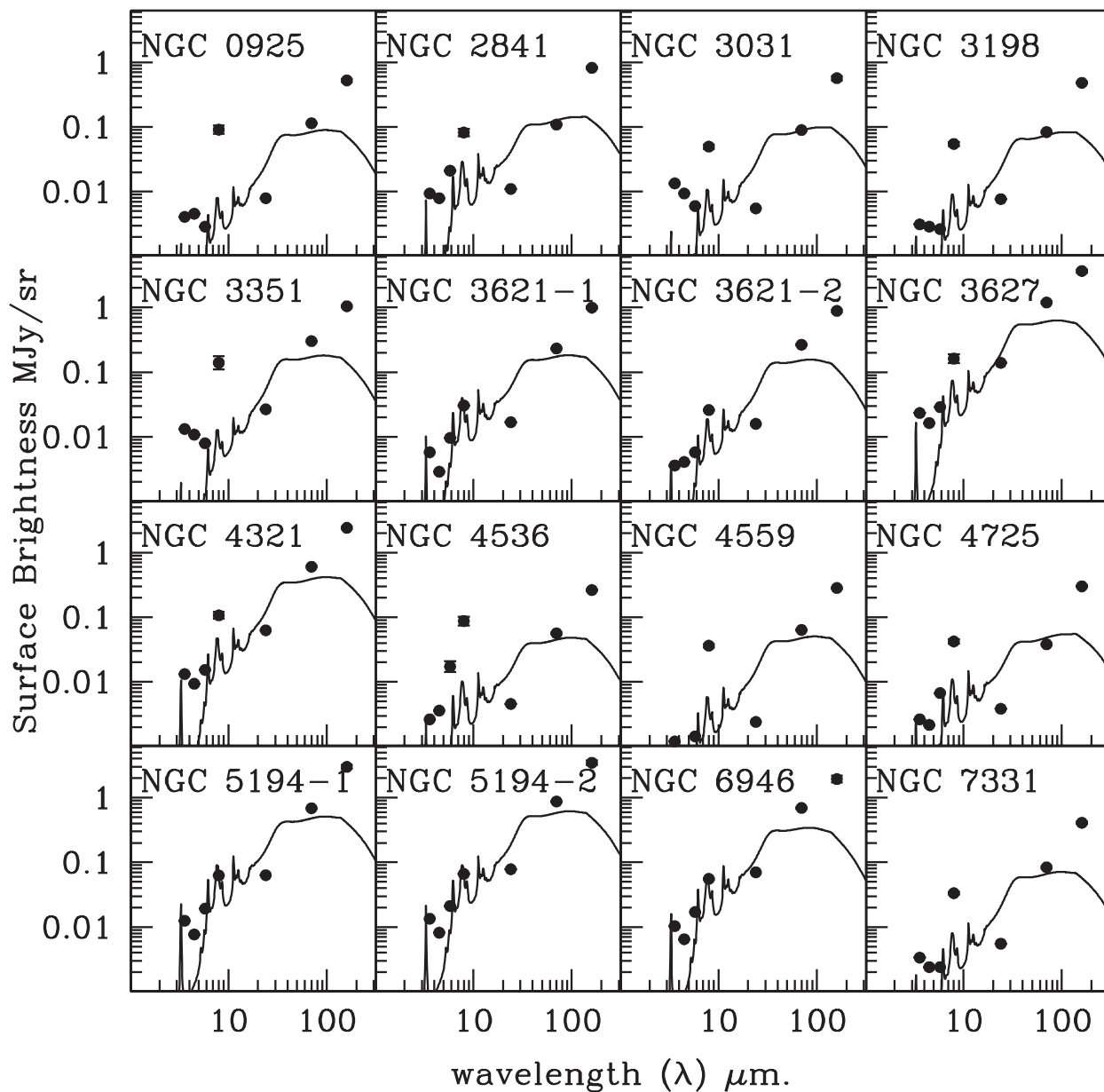


Fig. 2.— The Spectral Energy Distribution in the 7 *Spitzer* bands (IRAC/MIPS), for each of the WFPC2 apertures in Figure 1. The best fitting model from Draine & Li (2007) is shown. The relevant parameters for each fit are in Table 3.

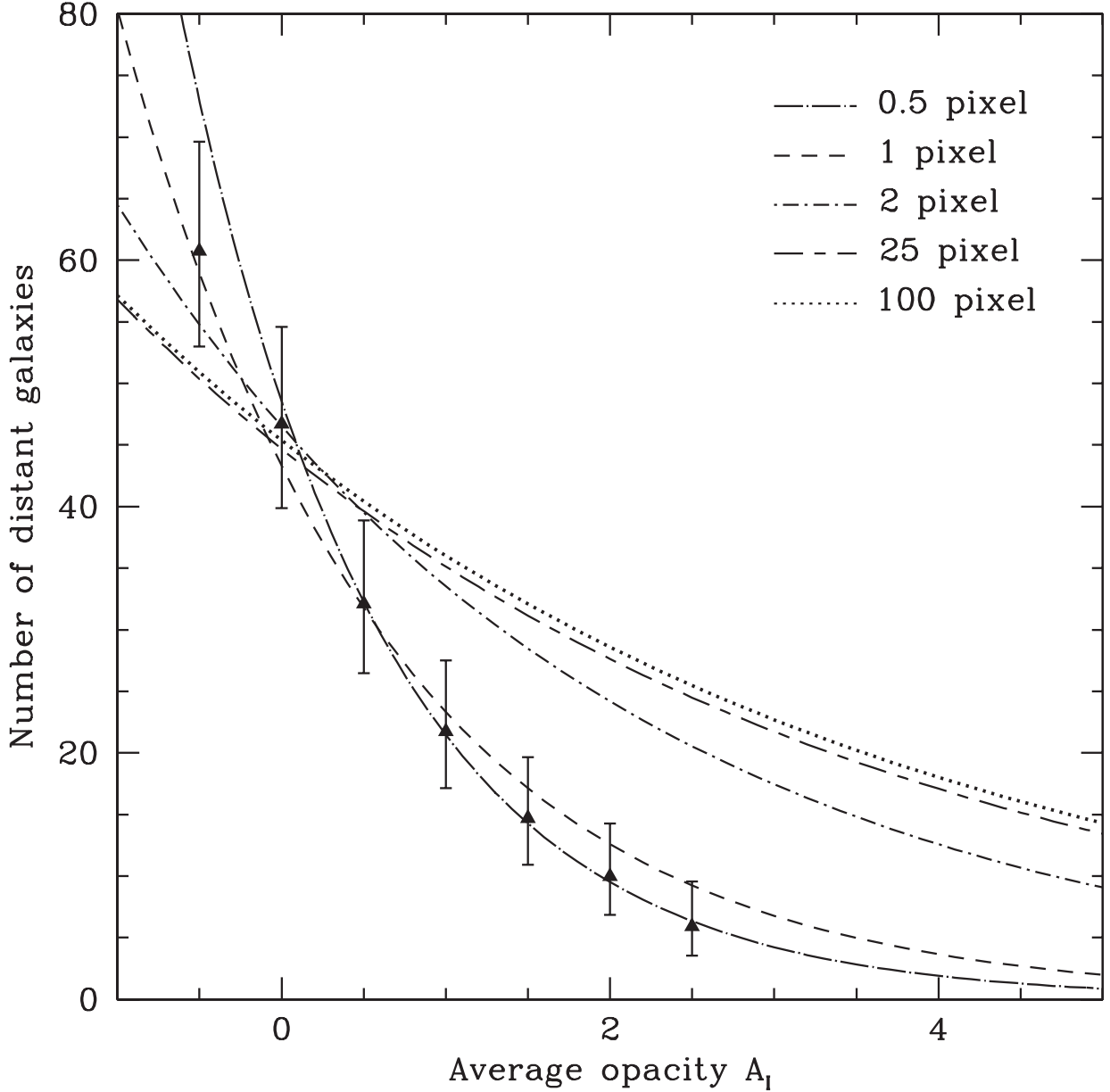


Fig. 3.— Different synthetic fields with different dust disk models from Holwerda (2005). A set of synthetic fields is made using dimmed HDF images. This dimming can be a smooth uniform gray screen (triangles), or some distribution of opaque clouds (curves). The relation between the number of distant galaxies from the HDF that can still be retrieved and the average opacity of the dimming depends on the assumed model. Large, resolved clouds block fewer background objects given the same filling factor. As a result, one a higher optical depth is implied by the intersection of the curve and number of observed background galaxies. The distance to NGC1365 is 18 Mpc, so a pixel of $0''.05$ is equivalent to 4 pc in linear size. The scales in the above simulations correspond, therefore, to clouds with cross-sections with a radius of 2, 4, 8, 100 and 400 pc, respectively

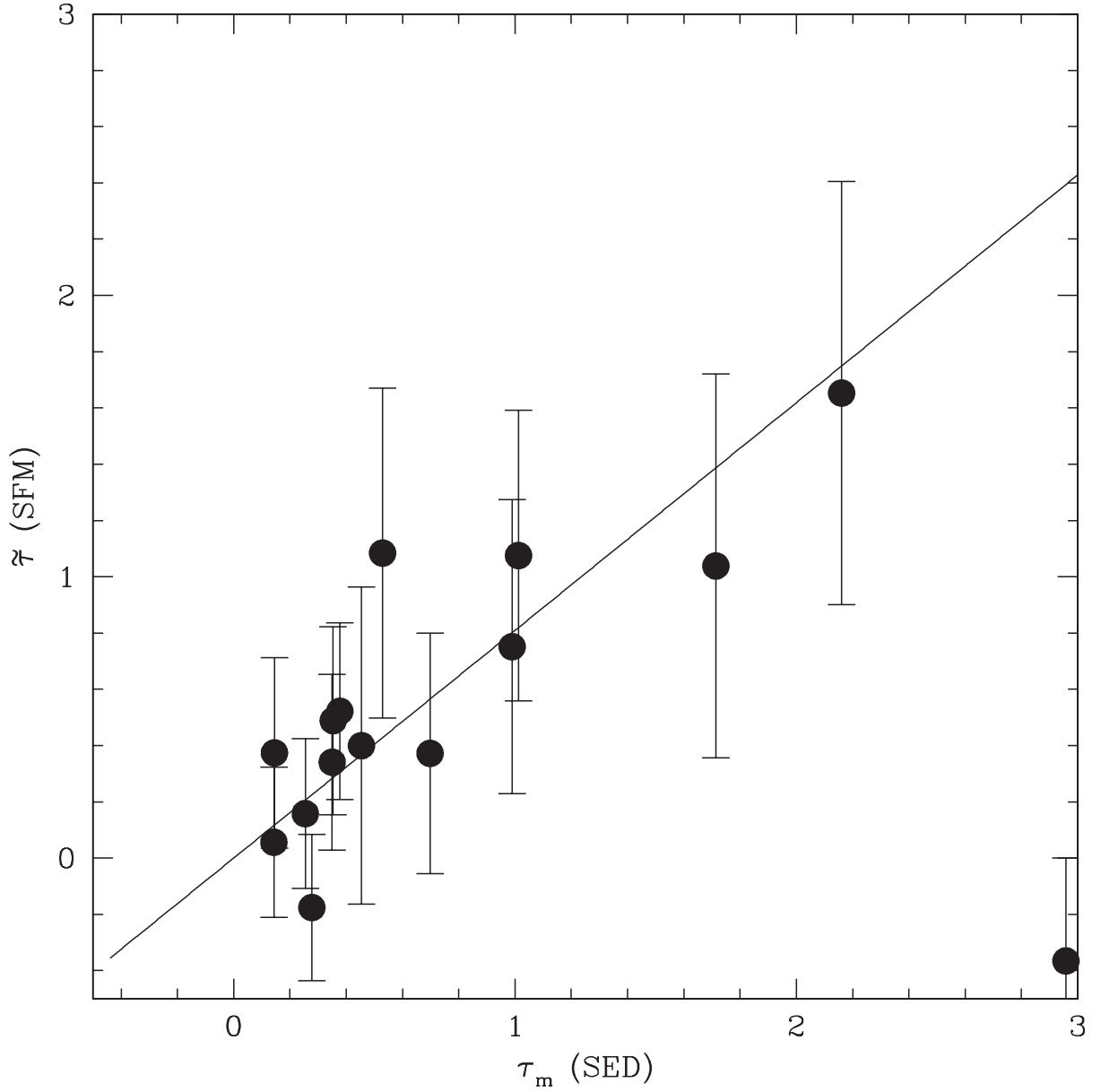


Fig. 4.— The mean and apparent optical depth in the I -band, from SED (τ_m) and SFM ($\tilde{\tau}$). The best fit with equation 6 to the ratios of these values is also shown ($\tau_c = 0.4$). The average value for number of clouds along the line-of-sight, n , is then 2.6. If the negative SFM values are included in the fit, the cloud optical depth rises to $\tau_c = 0.6$ and the average n becomes 1.9.

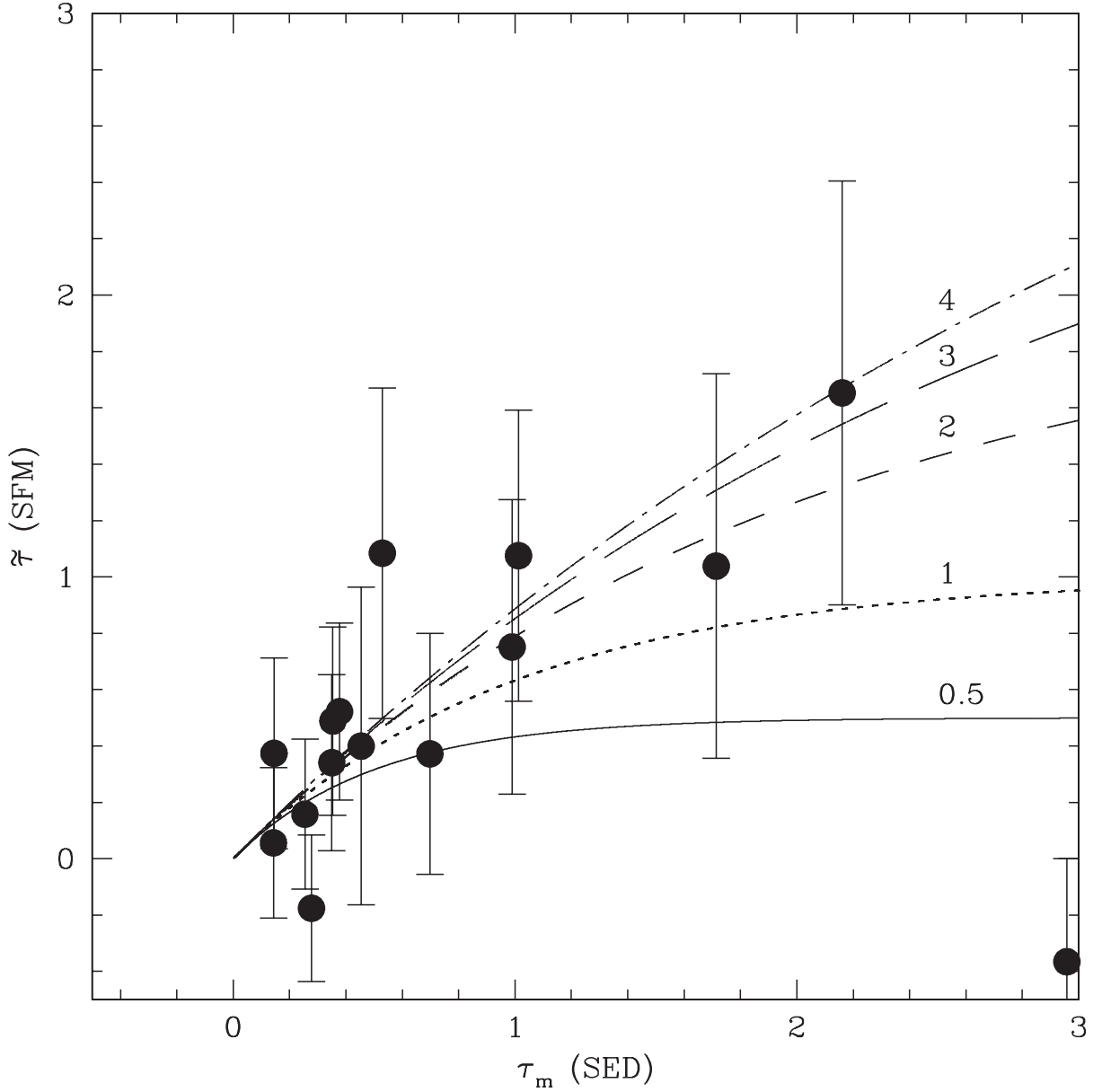


Fig. 5.— Model values of τ_m and $\tilde{\tau}$, from equations 2 and 3, for fixed values of the average number of clouds along the line-of-sight ($n = 0.5, 1, 2, 3, 4$). The cloud optical depth τ_c is left to vary proportionally to τ_m ($\tau_m = n \times \tau_c$, equation 2). Hence maximum cloud optical depths are 6, 3, 1.5, 1 and 0.75 respectively. If optically thin clouds are made up of optically thin clouds, it seems necessary that more than one cloud will lie along the line-of-sight.

Table 1. SINGS data description. IRAC and MIPS pixel scales, PSF FWHM, and aperture corrections (the factor by which the fluxes are multiplied).

Instrument (band)	pixel scale 1	PSF (FWHM) 2	aperture correction 3
IRAC (3.6)	0".75	2".5	0.9
IRAC (4.5)	0".75	2".5	0.9
IRAC (5.8)	0".75	2".5	0.7
IRAC (8.0)	0".75	2".5	0.75
MIPS (24)	1".5	6".0	1.16
MIPS (70)	4".5	18".0	1.2
MIPS (160)	9".0	40".0	1.4

¹Pixel scales were set by the SINGS team.

²FWHM values for the IRAC are conservative estimates. Actual FWHM values are better than 2".5.

³The IRAC values are the initial results from T. Jarrett (*private communication*), but they do not differ substantially from the final results.

Table 2. *Spitzer* channel surface brightness in the WFPC2 aperture ($3 \text{ WFs} \times 1.3' \times 1.3'$).

Galaxy	$3.6 \mu\text{m}$ MJy/sr	$4.5 \mu\text{m}$ MJy/sr	$5.8 \mu\text{m}$ MJy/sr	$8 \mu\text{m}$ MJy/sr	$24 \mu\text{m}$ MJy/sr	$70 \mu\text{m}$ MJy/sr	$160 \mu\text{m}$ MJy/sr
NGC 925	0.17 ± 0.04	0.19 ± 0.08	0.12 ± 0.05	3.79 ± 2.65	0.33 ± 0.06	4.76 ± 0.44	21.92 ± 0.91
NGC 2841	0.39 ± 0.04	0.33 ± 0.09	0.88 ± 0.59	3.42 ± 2.43	0.46 ± 0.04	4.54 ± 0.34	34.27 ± 0.58
NGC 3031	0.56 ± 0.03	0.39 ± 0.06	0.25 ± 0.07	2.07 ± 1.41	0.23 ± 0.04	3.74 ± 0.37	23.73 ± 1.38
NGC 3198	0.13 ± 0.02	0.12 ± 0.04	0.11 ± 0.04	2.28 ± 1.20	0.32 ± 0.05	3.48 ± 0.36	20.09 ± 0.46
NGC 3351	0.55 ± 0.05	0.45 ± 0.16	0.33 ± 0.07	5.81 ± 4.14	1.11 ± 0.06	12.54 ± 0.54	43.55 ± 0.68
NGC 3621-1	0.24 ± 0.01	0.12 ± 0.01	0.40 ± 0.05	1.27 ± 0.37	0.70 ± 0.05	9.68 ± 0.46	41.38 ± 0.87
NGC 3621-2	0.15 ± 0.01	0.17 ± 0.01	0.24 ± 0.05	1.08 ± 0.37	0.66 ± 0.05	11.04 ± 0.46	36.81 ± 0.87
NGC 3627	0.97 ± 0.04	0.68 ± 0.06	1.20 ± 0.06	6.72 ± 2.89	5.80 ± 0.06	49.58 ± 0.61	152.63 ± 0.95
NGC 4321	0.55 ± 0.02	0.39 ± 0.04	0.64 ± 0.06	4.45 ± 2.23	2.62 ± 0.05	25.12 ± 0.46	100.53 ± 0.75
NGC 4536	0.11 ± 0.04	0.15 ± 0.07	0.72 ± 3.45	3.64 ± 2.89	0.19 ± 0.05	2.35 ± 0.52	10.97 ± 0.60
NGC 4559	0.05 ± 0.03	0.04 ± 0.01	0.06 ± 0.05	1.51 ± 1.05	0.10 ± 0.05	2.65 ± 0.38	11.80 ± 0.53
NGC 4725	0.11 ± 0.02	0.09 ± 0.05	0.28 ± 0.20	1.76 ± 1.29	0.16 ± 0.05	1.59 ± 0.35	12.50 ± 0.49
NGC 5194-1	0.52 ± 0.01	0.32 ± 0.01	0.80 ± 0.05	2.61 ± 0.22	2.64 ± 0.04	28.61 ± 0.38	124.68 ± 1.36
NGC 5194-2	0.56 ± 0.01	0.34 ± 0.01	0.88 ± 0.05	2.76 ± 0.22	3.26 ± 0.04	36.35 ± 0.38	144.30 ± 1.36
NGC 6946	0.43 ± 0.03	0.27 ± 0.01	0.71 ± 0.09	2.31 ± 0.48	2.92 ± 0.07	28.88 ± 0.53	80.83 ± 2.13
NGC 7331	0.14 ± 0.01	0.10 ± 0.01	0.10 ± 0.05	1.39 ± 0.88	0.23 ± 0.04	3.49 ± 0.67	17.05 ± 0.79

Table 3. Model output: stellar and dust surface brightness, dust surface density, dust mean temperature (T_2 in Draine & Li 2007), fit quality, the parameters of stellar irradiation –minimum and maximum of the distribution, mean irradiative field, fraction of dust exposed to more than U_{min} . Models can be found at <http://www.astro.princeton.edu/~draine/dust/irem.html>

Galaxy name	$L_{star}/area$ (L_{\odot}/kpc^2) $\times 10^8$	$L_{dust}/area$ (L_{\odot}/kpc^2) $\times 10^8$	$M_{dust}/area$ (M_{\odot}/kpc^2) $\times 10^6$	T (K)	χ^2	U_{min}	U_{max} $\times 10^6$	\bar{U}	γ $\times 10^{-3}$	model name
NGC 0925	0.8	0.2	0.2	15.7	2.8	0.70	10	0.8	5.8	U0.70_1e7_MW3.1_20
NGC 2841	1.8	0.3	0.5	14.6	4.15	0.70	10	0.8	1.0	U0.70_1e7_MW3.1_20
NGC 3031	2.7	0.2	0.3	14.6	2.32	0.50	1.0	0.5	1.5	U0.50_1e6_MW3.1_30
NGC 3198	0.6	0.2	0.3	15.0	3.73	0.50	10	0.6	7.5	U0.50_1e7_MW3.1_30
NGC 3351	2.7	0.5	0.4	16.2	1.9	0.80	1.0	1.0	1.6	U0.80_1e6_MW3.1_10
NGC 3621-1	0.7	0.5	0.4	16.2	2.45	1.00	1.0	1.0	2.6	U1.00_1e6_MW3.1_60
NGC 3621-2	0.7	0.4	0.2	16.9	10.91	1.20	10	1.3	7.3	U1.20_1e7_MW3.1_30
NGC 3627	3.7	2.1	1.1	17.0	2.11	1.00	10	1.4	24.5	U1.00_1e7_MW3.1_30
NGC 4321	2.2	1.1	1.0	16.0	1.91	0.70	10	0.9	15.6	U0.70_1e7_MW3.1_30
NGC 4536	0.5	0.1	0.1	15.7	2.32	0.80	10	0.8	2.7	U0.80_1e7_MW3.1_60
NGC 4559	0.2	0.1	0.1	15.7	1.76	0.80	1.0	0.8	0.0	U0.80_1e6_MW3.1_30
NGC 4725	0.5	0.1	0.2	14.6	3.01	0.50	1.0	0.5	0.0	U0.50_1e6_MW3.1_60
NGC 5194-1	1.6	1.4	1.2	16.0	2.33	0.80	1.0	0.9	9.9	U0.80_1e6_MW3.1_50
NGC 5194-2	1.8	1.7	1.4	16.0	1.83	0.80	1.0	0.9	11.7	U0.80_1e6_MW3.1_40
NGC 6946	1.4	1.2	0.5	17.8	0.65	1.50	1.0	1.9	20.5	U1.50_1e6_MW3.1_50
NGC 7331	0.6	0.2	0.2	15.4	2.15	0.70	10	0.7	4.5	U0.70_1e7_MW3.1_30

Table 4. The apparent ($\tilde{\tau}$) and average (τ_m) optical depths in I -band measured in the WFPC2 field (3 WFs $1'.3 \times 1'.3$), uncorrected and corrected for inclination.

Galaxy	$\tilde{\tau}$ (SFM)	$\tilde{\tau}$ $\times \cos(i)$	τ_m (SED)	τ_m $\times \cos(i)$	$\tilde{\tau}/\tau_m$
NGC 0925	$-0.4_{-0.3}^{0.3}$	-0.2	0.6	0.3	-0.63
NGC 2841	$0.7_{-0.4}^{0.4}$	0.4	1.4	0.7	0.53
NGC 3031	$0.8_{-0.6}^{0.5}$	0.4	0.9	0.5	0.88
NGC 3198	$0.7_{-0.3}^{0.3}$	0.3	0.7	0.4	0.97
NGC 3351	$1.1_{-0.5}^{0.5}$	1.1	1.0	1.0	1.06
NGC 3621-1	$2.0_{-0.6}^{0.5}$	1.1	1.0	0.5	2.05
NGC 3621-2	$1.0_{-0.3}^{0.3}$	0.5	0.7	0.4	1.38
NGC 3627	$1.9_{-0.7}^{0.6}$	1.0	3.1	1.7	0.61
NGC 4321	$2.2_{-0.8}^{0.7}$	1.7	2.8	2.2	0.76
NGC 4536	$0.8_{-0.3}^{0.3}$	0.4	0.3	0.1	2.58
NGC 4559	$0.1_{-0.3}^{0.3}$	0.1	0.3	0.1	0.39
NGC 4725	$0.7_{-0.3}^{0.3}$	0.5	0.5	0.4	1.38
NGC 5194-1	$-0.4_{-0.4}^{0.4}$	-0.4	3.3	3.0	-0.12
NGC 5194-1	$1.3_{-0.6}^{0.5}$	1.2	3.9	3.5	0.34
NGC 6946	$1.0_{-0.5}^{0.5}$	0.8	1.3	1.0	0.76
NGC 7331	$0.3_{-0.3}^{0.3}$	0.2	0.5	0.3	0.62